Journal of
Materials Chemistry A

Accepted Manuscript

This article can be cited before page numbers have been issued, to do this please use: J. Wang, Z. Wu, L. Han, R. Lin, W. Xiao, C. Xuan, H. L. Xin and D. Wang, *J. Mater. Chem. A*, 2016, DOI: 10.1039/C6TA00490C.

ROYAL SOCIETY OF CHEMISTRY

www.rsc.org/materialsA

View Article Online
DOI: 10.1039/C6TA00490C

Journal of Materials Chemistry A

ARTICLE

Nitrogen and Sulfur Co-doping of Partially Exfoliated MWCNTs as Three Dimensional Structured Electrocatalyst for the Oxygen Reduction Reaction

Received 00th January 20xx,
Accepted 00th January 20xx

DOI: 10.1039/x0xx00000x

www.rsc.org/

Jie Wang,[a] Zexing Wu,[a] Lili Han,[b,c] Ruoqian Lin,[b,d] Weiping Xiao,[a] Cuijuan Xuan,[a] Huolin. L Xin,[b,d] and Deli Wang[a]*

Preventing the stacking of graphene sheets is of vital importance for highly efficient and stable fuel cell electrocatalysts. In the present work, we report a 3-D structured carbon nanotube intercalated graphene nanoribbon with N/S co-doping. The nanocomposite is obtained by high temperature heat-treated thiourea with partially unzipped multi-walled carbon nanotubes. The unique structure reserves both the properties of carbon nanotube and graphene, exhibiting excellent catalytic performance for the ORR with similar onset and half-wave potential relative to that of Pt/C electrocatalysts. Moreover, the stereo structured composite exhibits distinct advantages in long-term stability and methanol poisoning tolerance in comparison to Pt/C.

Introduction

Heteroatom (e.g. B [1, 2], N [3, 4], P [5, 6], S [7, 8] and I [9]) doped carbon materials as efficient noble metal-free catalysts have, to a certain extent, enhanced the kinetics of the oxygen reduction reaction (ORR) and reduced the cost compared with commercial Pt/C in alkaline solution. Currently, co-doping of heteroatoms into carbon materials as ORR catalysts have been further investigated to improve electrocatalytic activity. Synergistic catalytic effect for the ORR could be acquired among different dopants through creating new non-electron-neutral sites [10, 11] in the materials. Among the heteroatom elements, S atom has brought particular interest and was found to easily replacing the C atom when co-doping with N [12, 13].

Graphene, a single-atom-thick hexagonally arrayed sp^2 carbon atoms bonded sheet, has attracted a great deal of interest in renewable energy conversion and storage devices due to its unique properties, especially ultrahigh specific surface area and superior electron conductivity [14-17]. However, graphene based two-dimensional catalysts suffer from an irreversible re-stacking of the nanosheets due to the strong π-interaction during thermal annealing process and electrochemical measurements [18-20]. The re-stacking would result in a lower surface area, limiting the mass transfer rate and even decreasing the catalytic activity as well as running stability. Great efforts have been devoted to preventing the re-stacking of graphene, such as inserting carbon nanospheres or multi-walled carbon nanotubes (MWCNTs) into graphene layers [21-23], growing graphene on hierarchical porous carbon materials [5, 24], conversion of graphene into three dimensional aerogel to form a stereo structure [25]. Recently, a carbon nanotube-graphene complex was obtained through unzipping of MWCNTs or few-walled carbon nanotubes [4, 26].

In this paper, we report nitrogen and sulfur co-doped 3-D structured carbon nanotubes/graphene nanoribbon composites. The unique structure was obtained by partially exfoliation of outer walls of MWCNTs, to forming graphene nanoribbons attached to intact inner walls of nanotubes. The ratio of graphene to nanotubes was controlled by tuning the amount of MWCNT and oxidizing agents. The internal nanotube skeletons effectively prevent the graphene nanoribbon from agglomeration during high temperature and electrochemical process. As a result, the N/S co-doped graphene/nanotubes composites exhibited a direct four-electron pathway for the ORR, which is comparable to Pt/C. Moreover, the dual-doped stereo structure of nanotubes/graphene nanoribbon composites exhibit distinct advantages in long-term stability and methanol poisoning tolerance relative to Pt/C.

[a] *Key Laboratory of Material Chemistry for Energy Conversion and Storage (Huazhong University of Science and Technology), Ministry of Education, Hubei Key Laboratory of Material Chemistry and Service Failure, School of Chemistry and Chemical Engineering, Huazhong University of Science and Technology, Wuhan, 430074, P.R. China. E-mail: wangdl81125@hust.edu.cn.*
[b] *Center for Functional Nanomaterials, Brookhaven National Laboratory, Upton, NY 11973, USA.*
[c] *School of Materials Science and Engineering, Tianjin University, Tianjin 300072, P.R. China.*
[d] *Department of Materials Science and Engineering, Stony Brook University, Stony Brook, NY, 11794, USA.*
Electronic Supplementary Information (ESI) available: [details of photographic images, FT-IR spectrum, TGA curves and additional electrochemical performance]. See DOI: 10.1039/x0xx00000x

View Article Online
DOI: 10.1039/C6TA00490C

Experimental Section

Preparation of graphene/nanotubes composites

The exfoliation of MWCNTs was prepared similar to Hummers method [26]. 2.0 g of MWCNT was added into a 500 mL three-necked round-bottomed flask filled with 300 mL of concentrated H_2SO_4. The mixture was continuously mechanical stirred for 12 h at room temperature. 6.0 g of $KMnO_4$ was then slowly added into the flask and mechanical stirred for 1 h, and then heated to 70 ^oC for 1 h. After cooling down to room temperature, the mixture was poured into a 3000 mL baker filled with 25 mL of H_2O_2 and 500 mL of ice. Resulting precipitate was obtained suction-filtered in air and washed with copious amounts of distilled water until the pH was 7 and then underwent a freeze-drying. The obtained material was denoted as CNT-3 (the mass ratio of MWCNT to $KMnO_4$ was 1:3). Similarly, by changing the ratio to 1:0, 1:2, 1:4 and 1:6, the materials were denoted as CNT-0, CNT-2, CNT-4 and CNT-6, respectively.

Preparation of N/S co-doped exfoliation MWCNT

0.1 g of partially unzipped CNTs mixed with 1.0 g of thiourea was grounded into fine powder in a mortar. The mixture was then heated at 900 °C for 2 h under flowing N_2 in a tube furnace to obtain nitrogen and sulfur co-doped MWCNTs (NSCNT-3). For comparison, NSCNT-0, NSCNT-2, NSCNT-4 and NSCNT-6 were also prepared using the same procedure.
The main text of the article should appear here with headings as appropriate.

Physical characterization

Powder X-ray diffraction (XRD) was conducted by using an X'Pert PRO diffractometer, and diffraction patterns were collected using Cu Ka (λ = 1.5406 Å) radiation at a scanning rate of 4 °/min. Thermal gravimetric analysis (TGA) was carried out on TA-Q500 Instrument with a heating rate of 5 °C/min. X-ray photoelectron spectroscopy (XPS) data were obtained using an AXIS-ULTRA DLD-600W Instrument. Fourier transform infrared (FT-IR) spectra of the samples were collected on VERTEX 70, BRUKER Inc. S/TEM images were obtained using aberration-corrected Hitachi HD2700C Scanning Transmission Electron Microscope operated at 200 keV. Raman spectra were taken by a LabRam HR800 spectrometer with a 532 nm laser excitation.

Electrochemical measurements

The electrochemical measurements were performed on a Autolab PGSTAT302N electrochemical workstation equipped with a high speed rotator from Pine Instruments in which a three-electrode system consisting of a glassy carbon working electrode (5 mm in diameter), a piece of carbon paper as counter electrode to eliminate the contamination from Pt, and reverse hydrogen electrode as reference electrode at room temperature (298 K) in 0.1 M KOH solution. 5 mg of samples was dispersed in 1 mL of isopropanol/Nafion hybrid solutions and ultrasonic dispersed to form homogeneous ink. 16 μL of ink was drop onto the glassy carbon substrate, and dried naturally. Pt/C electrode with Pt mass loading of 15 μL cm^{-2} on GC electrode serves as working electrode for comparison. The cyclic voltammetry (CV) and linear sweep voltammetry (LSV) of the samples was operated in N_2- or O_2-saturated 0.1 M KOH solution at a scanning rate of 50 mV s^{-1} for CV and 5 mV s^{-1} for LSV measurements. Electrons transfer number (*n*) was calculated from the following Koutecky-Levich (K-L) equation:
The main text of the article should appear here with headings as appropriate.

$$\frac{1}{I}=\frac{1}{I_K}+\frac{1}{I_D} \quad (1)$$

$$I_D=0.62nFAD^{2/3}\omega^{1/2}\nu^{-1/6}C_{O_2} \quad (2)$$

Rotating ring-disc electrode (RRDE) measurements were performed in O_2-saturated 0.1 M KOH solution at a sweep rate of 5 mV s^{-1}. The ring potential was set as 1.2 V and the electron transfer number (n) and HO_2^- yield were calculated by using equation (3) and (4). The collection efficiency (N) was calibrated with and without a thin active layer on the disk via Fe^{2+}/Fe^{3+} couple in a 10 mM $K_3[Fe(CN)_6]$ solution. After calibration, the value of N was calculated to be 0.37.

$$n=\frac{4I_D}{I_D+\frac{I_R}{N}} \quad (3)$$

$$H_2O_2\%=\frac{\frac{2I_R}{N}}{I_D+\frac{I_R}{N}}\times 100\% \quad (4)$$

In the four equations, I, I_K, I_D represent the measured current, kinetic current and limiting diffusion current, respectively, n is the overall electrons transfer number, F is the Faraday constant (96 485 C mol^{-1}), A is the electrode area (A = 0.196 cm^2), D is the O_2 diffusion coefficient (D = 1.9×10^{-5} cm^2 s^{-1}), ν is the kinematic viscosity of the electrolyte (ν = 1.13×10^{-2} cm^2 s^{-1}), ω is the rotating speed of RDE, C_{O2} is the concentration of O_2 (C_{O2} = 1.2×10^{-3} mol L^{-1}). Before adding the data into the equation, rotating speed was converted from rpm into rad s^{-1}.

Results and discussion

Due to the harsh oxidizing of $KMnO_4$ and concentrated H_2SO_4, the process of MWCNT unzipping would introduce plenty of oxygen functional groups and defects. Thus, the exfoliation degree of MWCNTs could be represented by the water dispersible ability, where, the more oxygen functional groups and defects, the better hydrophilic. The water dispersible ability for carbon nanotubes with different exfoliation degrees are shown in the photograph illustrations (Figure S1). By adding 5.0 mg of samples into the vials separately, the five samples display gradient dispersible capabilities from non-

View Article Online
DOI: 10.1039/C6TA00490C

dispersible to easily dispersible property. After ultrasound for 60 s, the five samples were successively standing for 15 min and 30 min. It can be seen that the CNT-0 barely dispersed in water and the dispersible ability was successively enhanced from CNT-2 to CNT-6. The XRD pattern (Figure 1a) exhibits the structural transformation of CNTs with different exfoliation degrees. The diffraction peak related to the (002) plane at around 26 ° gradually disappeared, while the peak intensity related to (001) plane of graphene oxide at around 10 ° was increasing, suggesting the increasing of the exfoliation degree of CNTs. It is worth noting that the (001) plane was evidently moved to low-angle region, indicating the enlargement of lamellar spacing. FT-IR spectrum (Figure S2) shows the gradually enhanced absorption peaks of C=O bond (1735 cm^{-1}), C=C bond (1622 cm^{-1}) and epoxy C-O bond (1228 cm^{-1}), respectively. The increased intensity of the three characteristic peaks represents the deepening of oxidation degree which is in consistent with the XRD patterns in Figure 1a.

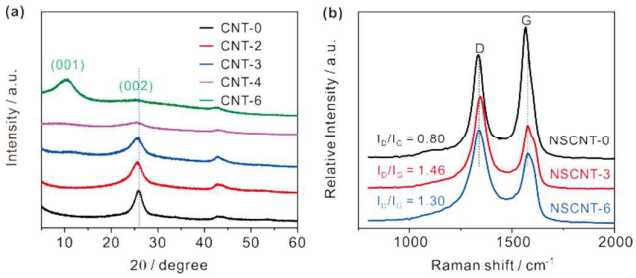

Figure 1. (a) XRD patterns of exfoliated CNT-0, CNT-2, CNT-3, CNT-4 and CNT-6; (b) Raman spectra of NSCNT-0, NSCNT-3 and NSCNT-6.

The morphology of the NSCNT materials were first characterized by scanning electron microscopy (SEM) measurement. The integrated one dimensional nanotube structure can be observed in Figure 2a. The defect-free structure hindered an adequate interaction of the inner tube-wall of NSCNT-0. A transition state morphology was obtained by partial exfoliation of MWCNTs. As shown in Figure 2b, the NSCNT-3 materials are in stereo structure with CNTs as skeleton supported exfoliated graphene nanoribbons. In an electrochemical condition, the interconnected structure could store electrolyte initially, providing a quick supply and short diffusion distance. On the contrary, due to the full unzipping of MWCNTs into graphene nanoribbons, the result NSCNT-6 experienced severe agglomeration because of the π-π re-stacking under high temperature calcination (Figure 2c). Raman spectra (Figure 1b) of all the three samples show characteristic D and G band located at 1350±20 cm^{-1} and 1575±20 cm^{-1}, respectively. The G band is attributed to the first order scattering of the E_{2g} mode of sp^2 carbon atoms, while the D band is induced by defects or disorder [27, 28]. Intensity ratio (I_D/I_G) of NSCNT-0, NSCNT-3 and NSCNT-6 were calculated to be 0.80, 1.46 and 1.30, respectively. The increasing of I_D/I_G was due to the partial exfoliation of MWCNTs, leaving many defects and disordered transition state. The following decrease of I_D/I_G from NSCNT-3 to NSCNT-6 indicated the strong π-π stacking and Van der Waals interactions between graphene nanoribbons layers, leading to stacking of nanoribbons and lowering the defects as well as disordered structures. Moreover, the G band of NSCNT-3 and NSCNT-6 slightly shift toward higher frequency with respect to that of NSCNT-0, indicating the successfully p-type doping of heteroatoms in the composite structure[29,30].

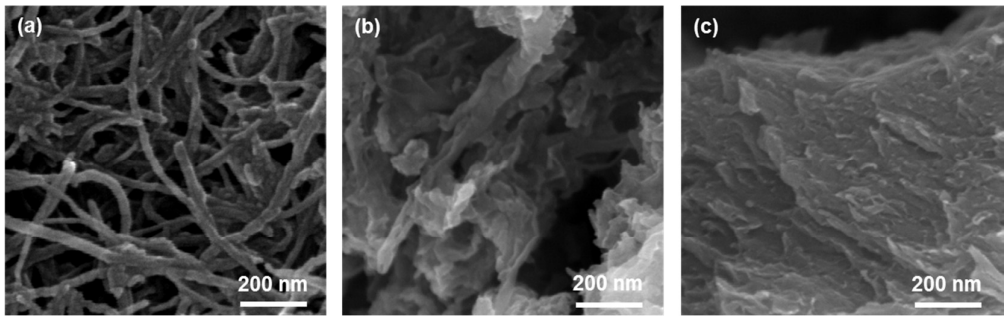

Figure 2. SEM images of NSCNT-0 (a), NSCNT-3 (b) and NSCNT-6 (c).

The transmission electron microscopy (TEM) image in Figure 3a shows the criss-cross of NSCNT-0 sample which maintained the integrated structure of MWCNTs after acid treatment. Figure 3b and 3d present the TEM images and HAADF-STEM images of NSCNT-3 sample. Most of the nanotubes are in looseness state with outer walls damaged and exfoliated, forming layered ribbon-like structures (yellow arrows in Figure 3b), which was different from NSCNT-0 in Figure 3a. Graphene nanoribbons were existed in two forms: i, distributed around the remained CNTs; ii, connected with the part of un-zipped CNTS. The internal nanotubes serve as support intercalated outward graphene nanoribbons, forming a three dimensional stereo structure and preventing the graphene layers from re-stacking when suffering from high temperature annealing. In contrast, NSCNT-6 shows severe re-stacked structure (Figure 3c) owning to the strong π-π stacking and Van der Waals interactions between graphene nanoribbons which is inconsistent with the SEM image in Figure 2c. From the corresponding HRTEM image (inset of Figure 3a and Figure 3b), it can be concluded that

View Article Online
DOI: 10.1039/C6TA00490C

the wall thickness (between the two red arrows) become thinner from NSCNT-0 to NSCNT-3. The d-spacing of NSCNT-3 between the layers in the tubes are no longer dense after harsh oxidation process. The nitrogen adsorption, desorption isotherms and pore size distribution were obtained at 77.3 K (Figure S3a and S3b) for NSCNT-0, NSCNT-3 and NSCNT-6. As a result, the specific surface area are 140.0 $m^2 g^{-1}$, 472.5 $m^2 g^{-1}$ and 322.3 $m^2 g^{-1}$ for NSCNT-0, NSCNT-3 and NSCNT-6 catalysts. Obvious hysteresis loop indicated mesoporous structure of the catalysts. Meanwhile, the three catalysts showed a similar pore size distribution at 6.4 nm which represent the remained CNTs, while NSCNT-3 exhibited another main pore size at 20 nm and NSCNT-6 exhibited two more main pore sizes distribution at 20 – 30 nm and 80 nm. Both the increasing of specific surface area and enlarging of pore size distribution would result in the improvement of ORR performance. Moreover, energy dispersive spectrometer (EDS) analysis of NSCNT-3 illustrates a homogenous distribution of N and S (Figure 3d-i). Considering that thiourea was completely decomposed above 600 ^{o}C, as shown in thermo gravimetric analysis (TGA) (Figure S4), N and S elements are proved to be doped into the exfoliated structure.

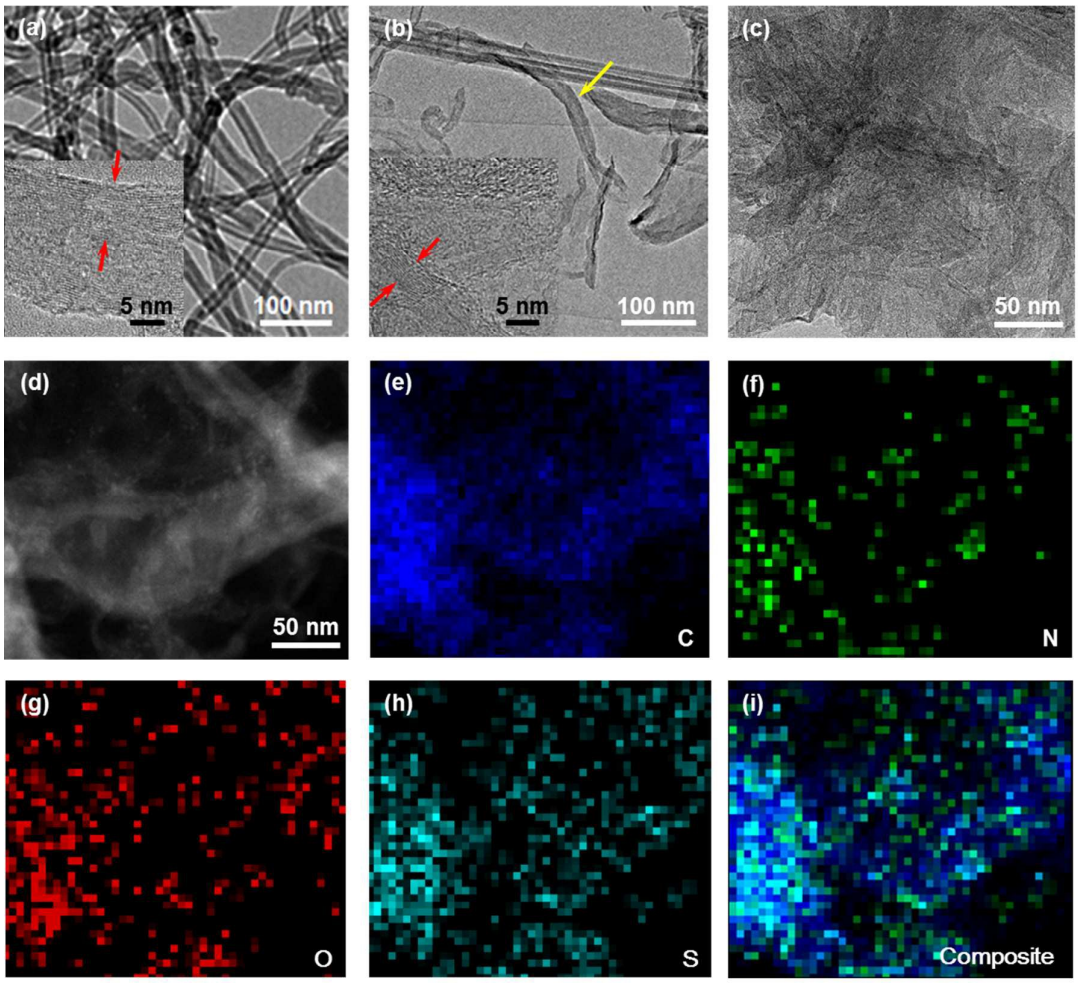

Figure 3. (a) TEM images of NSCNT-0 and the corresponding HR-TEM image (inset); (b) TEM image of NSCNT-3 and the corresponding HR-TEM image (inset); (c) TEM image of NSCNT-6; (d) High-angle annular dark field (HAADF)-STEM image of NSCNT-3 with the corresponding carbon (e), nitrogen (f), oxygen (g), sulfur (h) and the composite (i) of EDS elemental mapping images.

The surface elemental composition of NSCNT-3 was determined by XPS analysis. As shown in Figure 4a, the XPS spectrum of NSCNT-3 exhibits five characteristic peaks located at ca. 165, 228, 285, 399 and 533 eV, corresponding to S 2p, S 2s, C 1s, N 1s, and O 1s[31], respectively. The elemental content of N and S for NSCNT-3 is 1.94% and 1.52%, respectively. The high-resolution spectrum of C 1s in NSCNT-3 (Figure 4b) was deconvoluted into six peaks. Among them, peaks at 283.9 eV and 287.2 eV are corresponding to C-S-C and C-N-C bond [21, 32, 33], further confirming that N and S atoms have been successfully doped into the stereo framework. Meanwhile, different oxygen containing groups, C-OH (285 eV), C=O (285.7 eV) and COOH (289.0 eV) were also observed in NSCNT-3. The high-resolution N1s spectrum (Figure 4c) shows three single N species peaks at 398.2 eV, 399.8 eV and 401.4 eV, corresponding to pyridinic N, pyrrolic N and graphitic N [34, 35], respectively. Moreover, NSCNT-3 contains S atoms that form three single peaks shown in Figure 4d at 163.8 eV, 165.0

View Article Online
DOI: 10.1039/C6TA00490C

eV and 168.8 eV, which are attributed to sulfur in C-S-C bonds, conjugated -C=S- and -SO_n- bonds [36, 37], respectively.

The electrochemical performance of the N/S dual-doped samples towards ORR was studied by cyclic voltammetry (CV) in N_2- and O_2-saturated 0.1 M KOH solution. In N_2- saturated KOH solution, there was no redox peaks, however, the CVs exhibit obvious oxygen reduction peaks in O_2 saturated solution (Figure S5). In addition, the NSCNT-3 shows a sharp oxygen reduction peak at 0.79 V, while the peak potential of NSCNT-0, NSCNT-2, NSCNT-4 and NSCNT-6 are at

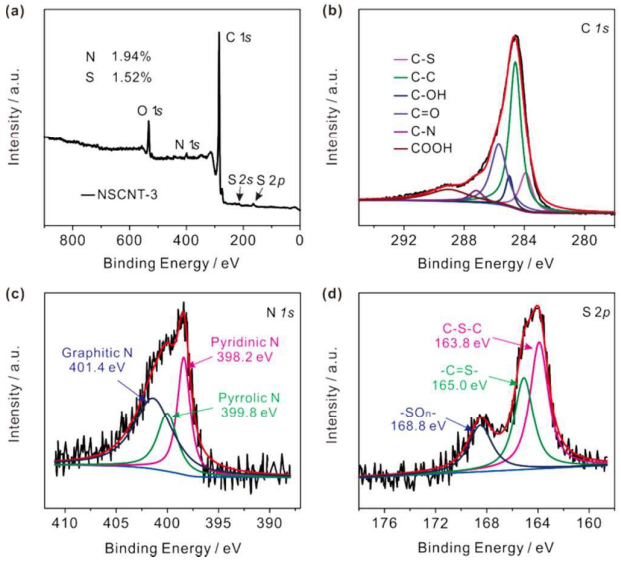

Figure 4. (a) XPS spectrum of NSCNT-3 and the corresponding high-resolution spectrum of C 1s (b), N 1s (c), and S 2p (d).

0.66 V, 0.75 V, 0.76 V and 0.75 V, respectively. The higher peak potential indicates better electrocatalytic activity of the NSCNT-3 towards ORR. To better understand the ORR catalytic activity of the samples, linear sweep voltammetry (LSV) measurement was conducted with Pt/C catalyst for comparison. Among the investigated samples, NSCNT-3 exhibits the best ORR activity in terms of onset and half wave potentials (0.97 V and 0.81 V vs. RHE) which were close to commercial Pt/C (0.96 V and 0.80 V, Figure 5a). However, NSCNT-4 showed well onset and half wave potential (0.97 V and 0.78 V) but lower limiting diffusion current density. The optimal limiting diffusion current density of NSCNT-3 (equal to Pt/C) was due to the three dimensional structure of carbon nanotube skeleton supported exfoliated graphene nanoribbons. The poor performance of NSCNT-6 was caused by the severe agglomeration of graphene nanoribbons after high temperature calcination procedure. Therefore, it is concluded that an appropriate exfoliation degree of MWCNT was necessary for superior ORR performance, while higher or inadequate exfoliation would result in poor catalytic activity. Figure 5b shows the Tafel plots of the five NSCNT samples and Pt/C by plotting the logarithm of the kinetic current density derived from the ORR curves. The kinetic current density was derived from equation 1. At low over-potentials, the Tafel slope of NSCNT-3 (67.1 mV dec^{-1}) is close to the Pt/C (69.1 mV dec^{-1}), indicating that NSCNT-3 undergoes the similar ORR mechanism with Pt/C: the protonation of O_2^- on the active sites of catalyst is the main rate-determining step [38-40].

The polarization curves for the ORR on NSCNT-3 at different rotation speeds are shown in Figure 5c. Due to the difference of O_2 diffusion rate on the electrode surface, the limiting diffusion current density increased when accelerating the rotation speeds. The inset of Figure 5c shows the Koutecky-Levich (K-L) plots (j vs. $\omega^{1/2}$) derived from equation (1) and (2) (analogous curves and K-L plots for NSCNT-4 are given in Figure S6), respectively. The three fitting straight lines show good linearity and demonstrate first-order ORR kinetics at these potentials [1, 41]. The electron transfer number (n) for NSCNT-3 was quantitatively calculated to be 3.86, 3.81 and 3.97 (at potentials of 0.7 V, 0.75 V and 0.80 V), while NSCNT-4 was 3.47, 3.51 and 3.65 (at potentials of 0.65 V, 0.70 V and 0.75 V) by using the slopes of these plots, indicating a 4-electron pathway dominated ORR process. To gain further insights into the ORR mechanism, rotating ring-disc electrode (RRDE) for the LSV measurement was conducted on NSCNT-3. The negligible ring current density (the oxidation of peroxide generated on the ring electrode, inset of Figure 5d) in comparison to the disc current density demonstrated little HO_2^- yield during the ORR process. The yield of HO_2^- and electrons transfer number (n) derived from the ring and disc current are presented in Figure 5d. Obviously, the HO_2^- yield and the electrons transfer number at a potential range from 0.1 V - 0.85 V on the NSCNT-3 were below 6 % and closed to 4, respectively, which are close to the RRDE results of Pt/C (Figure S7). The optimal negligible HO_2^- yield and near 4-electron transfer number suggested a 4-electron reaction dominant pathway and was in consistent with the RDE results.

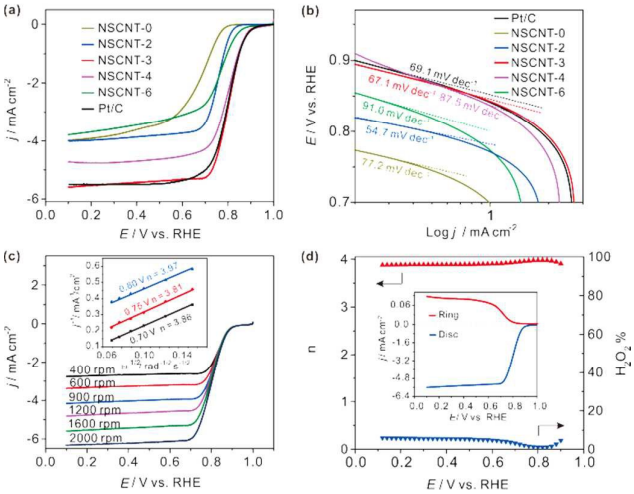

Figure 5. (a) ORR polarization curves of NSCNT samples and Pt/C at a rotation speed of 1600 rpm in O_2-saturated 0.1 M KOH solution; (b) Tafel plots of ORR polarization curves of (a); (c) ORR polarization curves of NSCNT-3 in O_2-saturated 0.1 M KOH solution at different rotating speed and its corresponding Koutecky-Levich plots under potentials of 0.65 V, 0.70 V and 0.75 V (inset); (d) The electron-transfer number n, H_2O_2 yield and RRDE voltammograms (inset) for NSCNT-3 catalyst.

View Article Online
DOI: 10.1039/C6TA00490C

Long-term catalytic stability and fuel crossover effect are important issues challenging the cathode catalysts in current fuel cell techniques [42-44]. The durability of NSCNT-3 was first evaluated by potential cycling between 0.05 and 1.0 V in O_2-saturated 0.1 M KOH solution at a scan rate of 200 mV s^{-1}. As shown in Figure 6a, the NSCNT-3 catalyst exhibited negligible oxygen reduction peak potential shift after 5000 and even 10,000 potential cycles, indicating superior catalytic stability. In addition, chronoamperometric measurements at constant potential of 0.7 V and rotation speed of 1600 rpm were performed in O_2-saturated solution. As shown in Figure 6a, the NSCNT-3 displayed slight activity loss while Pt/C suffered from gradually activity fading and only 64 % current remaining after 15000 s. These results indicate a much better stability of NSCNT-3 than Pt/C catalyst in alkaline media. The CV curves (Figure S8) of Pt/C electrode in the presence of 1 M methanol showed two characteristic oxidation peaks at 0.94 V and 0.78 V, which represent the methanol oxidation peak and CO oxidation peak[45], respectively. The methanol oxidation reaction and oxygen reduction reaction created a competitive relationship which would, to a certain degree, decrease the oxygen reduction activity. While the CV curves of before and after adding 1 M methanol for NSCNT-3 exhibited no obvious change in O_2-saturated solution, suggesting better methanol tolerance. Figure 6c compared the ORR polarization curves on NSCNT-3 and Pt/C electrode in O_2-saturated 0.1 M KOH in the presence of 1 M methanol at a rotation rate of 1600 rpm. NSCNT-3 showed negligible activity with and without 1 M methanol. However, Pt/C exhibited an obvious oxidation peak at about 0.7 V and significantly negative shift of half-wave potential about 250 mV, indicating severe ORR activity loss in presence of methanol. Moreover, potentiostat curves at 0.7 V was conducted for NSCNT-3 and Pt/C by injected 1 M methanol into the solution at 400 s (Figure 6d). NSCNT-3 showed slight fluctuation and remains stable current response while Pt/C suffered a sharp loss of 23.5 % activity. These results indicate the better catalytic stability and methanol tolerance of NSCNT-3 than commercial Pt/C catalyst which is suitable as cathode catalyst for alkaline fuel cells.

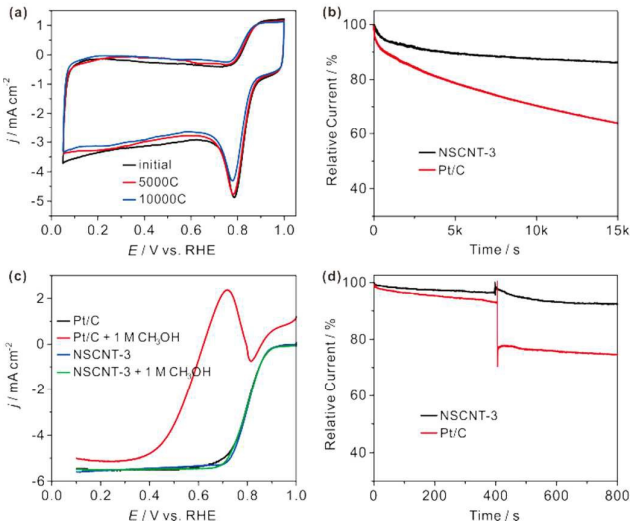

Figure 6. (a) Cyclic voltammetry curves of NSCNT-3 in O_2-purged 0.1 M KOH solution at room temperature for various numbers of potential cycles; (b) i-t chronoamperometric stability measurement (at a potential of 0.7 V) of NSCNT-3 and Pt/C in O_2-saturated 0.1 M KOH solution at a rotating speed of 1600 rpm; (c) Polarization curves of NSCNT-3 and Pt/C in O_2-saturated 0.1 M KOH solution and the presence of 1 M methanol; (d) Methanol crossover tests for NSCNT-3 catalyst performed on RDE with a rotation rate of 1600 rpm by injecting methanol into the electrolyte to reach a concentration of 1 M.

Conclusions

In summary, nitrogen and sulfur co-doped 3-D structured carbon nanotubes/graphene nanoribbon composites have been successfully prepared. The internal nanotube skeletons effectively prevent the outward graphene nanoribbons from accumulation under high temperature and electrochemical process. The unique stereo structure and efficient N/S co-doping favor the adequate penetration with electrolyte and provide more active sites for the ORR. NSCNT-3 showed excellent catalytic activity including a highly positive onset potential and half-wave potential which is similar to Pt/C catalyst. Moreover, the NSCNT-3 catalyst exhibited superior stability and methanol tolerance capability which made great improvement compared with Pt-based catalysts.

Acknowledgements

This work was supported by the National Natural Science Foundation (21306060, 21573083), the Program for New Century Excellent Talents in Universities of China (NCET-13-0237), the Fundamental Research Funds for the Central University (2013TS136, 2014YQ009). The authors thank the Analytical and Testing Center of HUST for XRD, STEM measurements.

Notes and references

1 Z.-H. Sheng, H.-L. Gao, W.-J. Bao, F.-B. Wang and X.-H. Xia, *J. Mater. Chem.*, 2012, **22**, 390-395
2 Y. Cheng, Y. Tian, X. Fan, J. Liu and C. Yan, *Electrochim. Acta*, 2014, **143**, 291-296.
3 T. Xing, Y. Zheng, L. H. Li, B. C. Cowie, D. Gunzelmann, S. Z. Qiao, S. Huang and Y. Chen, *ACS Nano*, 2014, **8**, 6856-6862.
4 Y. Li, W. Zhou, H. Wang, L. Xie, Y. Liang, F. Wei, J.-C. Idrobo, S. J. Pennycook and H. Dai, *Nat. Nanotechnol.*, 2012, **7**, 394-400.
5 J. Liang, X. Du, C. Gibson, X. W. Du and S. Z. Qiao, *Adv. Mater.*, 2013, **25**, 6226-6231.
6 J. Wu, C. Jin, Z. Yang, J. Tian and R. Yang, *Carbon*, 2015, **82**, 562-571.
7 Z. Yang, Z. Yao, G. Li, G. Fang, H. Nie, Z. Liu, X. Zhou, X. a. Chen and S. Huang, *ACS Nano*, 2011, **6**, 205-211.
8 Y. Zhang, M. Chu, L. Yang, W. Deng, Y. Tan, M. Ma and Q. Xie, *Chem. Commun.*, 2014, **50**, 6382-6385.
9 Z. Yao, H. Nie, Z. Yang, X. Zhou, Z. Liu and S. Huang, *Chem. Commun.*, 2012, **48**, 1027-1029.

View Article Online
DOI: 10.1039/C6TA00490C

10 D. C. Higgins, M. A. Hoque, F. Hassan, J.-Y. Choi, B. Kim and Z. Chen, *ACS Catal.*, 2014, **4**, 2734-2740.
11 M. Favaro, L. Ferrighi, G. Fazio, L. Colazzo, C. Di Valentin, C. Durante, F. Sedona, A. Gennaro, S. Agnoli and G. Granozzi, *ACS Catal.*, 2014, **5**, 129-144.
12 P. A. Denis, C. P. Huelmo and F. Iribarne, *Comput. Theor. Chem.*, 2014, **1049**, 13-19.
13 W. Ai, Z. Luo, J. Jiang, J. Zhu, Z. Du, Z. Fan, L. Xie, H. Zhang, W. Huang and T. Yu, *Adv. Mater.*, 2014, **26**, 6186-6192.
14 Y. Li, Y. Zhao, H. Cheng, Y. Hu, G. Shi, L. Dai and L. Qu, *J. Am. Chem. Soc.*, 2011, **134**, 15-18.
15 J. Duan, S. Chen, S. Dai and S. Z. Qiao, *Adv. Funct. Mater.*, 2014, **24**, 2072-2078.
16 W. Wang, L. Hu, J. Ge, Z. Hu, H. Sun, H. Sun, H. Zhang, H. Zhu and S. Jiao, *Chem. Mater.*, 2014, **26**, 3721-3730.
17 G. Zhang, B. Y. Xia and X. Wang, *Adv. Mater.*, 2014, **26**, 2408-2412.
18 S. Yang, L. Zhi, K. Tang, X. Feng, J. Maier and K. Müllen, *Adv. Funct. Mater.*, 2012, **22**, 3634-3640.
19 B. Xia, Y. Yan, X. Wang and X. W. D. Lou, *Mater. Horiz.*, 2014, **1**, 379-399.
20 Q. Cheng, J. Tang, N. Shinya and L.-C. Qin, *J. Power Sources*, 2013, **241**, 423-428.
21 M. Wu, J. Wang, Z. Wu, H. L. Xin and D. Wang, *J. Mater. Chem. A*, 2015, **3**, 7727-7731.
22 P. Chen, T. Y. Xiao, Y. H. Qian, S. S. Li and S. H. Yu, *Adv. Mater.*, 2013, **25**, 3192-3196.
23 C. H. Choi, M. W. Chung, H. C. Kwon, J. H. Chung and S. I. Woo, *Appl. Catal. B: Environ.*, 2014, **144**, 760-766.
24 J. Xu, K. Wang, S.-Z. Zu, B.-H. Han and Z. Wei, *ACS Nano*, 2010, **4**, 5019-5026.
25 H. Yin, C. Zhang, F. Liu and Y. Hou, *Adv. Funct. Mater.*, 2014, **24**, 2930-2937.
26 D. V. Kosynkin, A. L. Higginbotham, A. Sinitskii, J. R. Lomeda, A. Dimiev, B. K. Price and J. M. Tour, *Nature*, 2009, **458**, 872-876.
27 L. Panchakarla, K. Subrahmanyam, S. Saha, A. Govindaraj, H. Krishnamurthy, U. Waghmare and C. Rao, *Adv. Mater.*, 2009, **21**, 4726-4730.
28 A. Das, S. Pisana, B. Chakraborty, S. Piscanec, S. Saha, U. Waghmare, K. Novoselov, H. Krishnamurthy, A. Geim and A. Ferrari, *Nat. Nanotechnol.*, 2008, **3**, 210-215.
29 D. Deng, X. Pan, L. Yu, Y. Cui, Y. Jiang, J. Qi, W.-X. Li, Q. Fu, X. Ma and Q. Xue, *Chem. Mater.*, 2011, **23**, 1188-1193.
30 F.-X. Ma, J. Wang, F.-B. Wang and X.-H. Xia, *Chem. Commun.*, 2015, **51**, 1198-1201.
31 J.-M. You, M. S. Ahmed, H. S. Han, J. eun Choe, Z. Üstündağ and S. Jeon, *J. Power Sources*, 2015, **275**, 73-79.
32 J. Liang, Y. Jiao, M. Jaroniec and S. Z. Qiao, *Angew. Chem. Int. Ed.*, 2012, **51**, 11496-11500.
33 W. S. V. Lee, M. Leng, M. Li, X. L. Huang and J. M. Xue, *Nano Energy*, 2015, **12**, 250-257.
34 J. Tai, J. Hu, Z. Chen and H. Lu, *RSC Adv.*, 2014, **4**, 61437-61443.
35 X. Duan, S. Indrawirawan, H. Sun and S. Wang, *Catal. Today*, 2015, **249**, 184-191.
36 Y. Su, Y. Zhang, X. Zhuang, S. Li, D. Wu, F. Zhang and X. Feng, *Carbon*, 2013, **62**, 296-301.
37 X. Wang, J. Wang, D. Wang, S. Dou, Z. Ma, J. Wu, L. Tao, A. Shen, C. Ouyang and Q. Liu, *Chem. Commun.*, 2014, **50**, 4839-4842.
38 Y. Zhao, J. Liu, Y. Zhao and F. Wang, *Phys. Chem. Chem. Phys.*, 2014, **16**, 19298-19306.
39 V. Stamenkovic, T. Schmidt, P. Ross and N. Markovic, *J. Phys. Chem. B*, 2002, **106**, 11970-11979.
40 B. Blizanac, P. Ross and N. Markovic, *J. Phys. Chem. B*, 2006, **110**, 4735-4741.
41 L. Lai, J. R. Potts, D. Zhan, L. Wang, C. K. Poh, C. Tang, H. Gong, Z. Shen, J. Lin and R. S. Ruoff, *Energy Environ. Sci.*, 2012, **5**, 7936-7942.
42 J. Jin, F. Pan, L. Jiang, X. Fu, A. Liang, Z. Wei, J. Zhang and G. Sun, *ACS Nano*, 2014, **8**, 3313-3321.
43 Y. Zhang, J. Ge, L. Wang, D. Wang, F. Ding, X. Tao and W. Chen, *Sci. Rep.*, 2013, **3**, 2771.
44 J. Wang, H. L. Xin, J. Zhu, S. Liu, Z. Wu and D. Wang, *J. Mater. Chem. A*, 2015, **3**, 1601-1608.
45 K. Eid, H. Wang, P. He, K. Wang, T. Ahamad, S. M. Alshehri, Y. Yamauchi and L. Wang, *Nanoscale*, 2015, **7**, 16860-16866.